Chemical Physics 532 (2020) 110695

Contents lists available at ScienceDirect

Chemical Physics

journal homepage: www.elsevier.com/locate/chemphys

Full-dimensional quantum dynamics of SO($X^3\Sigma^-$) in collision with H_2

Benhui Yang[a,*], P. Zhang[b], C. Qu[c,f], P.C. Stancil[a], J.M. Bowman[c], N. Balakrishnan[d], R.C. Forrey[e]

[a] Department of Physics and Astronomy and Center for Simulational Physics, University of Georgia, Athens, GA 30602, USA
[b] Department of Chemistry, Duke University, Durham, NC 27708, USA
[c] Department of Chemistry, Emory University, Atlanta, GA 30322, USA
[d] Department of Chemistry and Biochemistry, University of Nevada, Las Vegas, NV 89154, USA
[e] Department of Physics, Penn State University, Berks Campus, Reading, PA 19610, USA
[f] Department of Chemistry and Biochemistry, University of Maryland, College Park, MD 20742, USA

ARTICLE INFO

Keywords:
SOH_2
Six-dimensional potential surface
Rovibrational transition
State-to-state cross section
Rate coefficient

ABSTRACT

A six-dimensional (6D) potential energy surface (PES) for the SO(X -HSO($X^3\Sigma^-$)-H_2 system is computed using high-level electronic structure theory and fit using a hybrid invariant polynomial method. Full-dimensional quantum close-coupling scattering calculations have been carried out using this potential for rotational and, for the first time, vibrational quenching transitions of SO induced by H_2. State-to-state cross sections and rate coefficients of SO are reported for rotational transitions from rotational levels $j_1 = 0$–10 in the ground vibrational state neglecting fine-structure. Some selected state-to-state rotational rate coefficients are compared with previous theoretical results obtained using a rigid-rotor approximation. For vibrational quenching, state-to-state and total cross sections and rate coefficients were calculated for the transitions in $SO(v_1 = 1, j_1) + H_2(v_2 = 0, j_2) \rightarrow SO(v_1' = 0, j_1') + H_2(v_2' = 0, j_2')$ collisions with $j_1 = 0$–5. Cross sections for collision energies in the range 1 to 3000 cm^{-1} and rate coefficients in the temperature range of 5–600 K are obtained for both para-H_2 ($j_2 = 0$) and ortho-H_2 ($j_2 = 1$) collision partners. The application of the results to astrophysics is discussed.

1. Introduction

Quantitative non-local thermodynamic equilibrium (NLTE) modeling of molecular excitation and spectral synthesis of cool astrophysical environments requires an extensive array of accurate molecular collisional rate coefficients. In cold molecular clouds, molecular collisions are the dominant factor in analysis of molecular emission and absorption, and H_2 is the most important collision partner because of its large abundance. A large portion of the collisional data, particularly for molecular vibrational excitations, are either currently unavailable or the available data are insufficient to meet the demands required by the modeling applications. However, due to the difficulty and complication of direct measurements of the collisional rate coefficients, astrophysical modeling mostly depends on theoretical calculations [1].

Sulfur monoxide (SO) was first observed in the interstellar gas by Gottlieb and Ball [2] and in cold dark clouds by Rydbeck et al. [3]. Since then, SO has been widely observed in the Orion molecular cloud [4], in low-mass star-forming regions [5], in high-mass star-forming regions [6], and in massive dense cores [7]. Very recently, Meier et al. [8] detected a significant number of sulfureted species, including CS and SO, in the central kiloparsec of the nearby starburst galaxy NGC 253, based on observations taken with the Atacama Large Millimeter/submillimeter Array. Using the IRAM 30 m telescope at Pico Veleta, SO rotational transitions were detected towards the star-forming regions W31C, G29.96-0.02, G34.3 + 0.1, W49N and W51 [9]. Velilla Prieto et al. [10] investigated the physical and chemical properties of the molecular envelope of the oxygen-rich asymptotic giant branch (AGB) star IK Tau and identified for the first time rotational lines of SO.

As far as we know, no theoretical or experimental rovibrational cross sections and rate coefficients of SO in collisions with H_2 are available. There have been a few theoretical studies of pure rotational transitions. Rotational excitation rate coefficients among fine-structure levels of SO in collisions with para-H_2 were calculated by Green [11] using a CS-H_2 interaction potential with the reduced mass of SO-H_2. Lique et al. [12] computed a four-dimensional (4D) potential for the SO ($X^3\Sigma^-$)-H_2 interaction using the restricted-spin coupled-cluster single-double plus perturbative triple excitation [RCCSD(T)] [13] theory with the aug-cc-pVTZ basis sets [14]. The potential was used in their scattering calculations of SO with para-H_2. However, the 4D potential was reduced to a 2D potential by averaging over θ_2 and ϕ with the assumption of H_2 being a structureless particle. As a result, the global minimum of the 2D potential is -93.81 cm^{-1} compared to the value of

* Corresponding author.
E-mail address: byang@uga.edu (B. Yang).

https://doi.org/10.1016/j.chemphys.2020.110695
Received 23 October 2019; Received in revised form 2 January 2020; Accepted 22 January 2020
Available online 25 January 2020
0301-0104/

about -157.00 cm^{-1} of the 4D potential. Collisional excitation cross sections and rate coefficients between the fine-structure states of SO with para-H_2 were performed at low temperatures using the averaged 2D potential. For scattering of vibrationally excited SO, rovibrational excitation of SO in collision with He was studied using the vibrational close-coupling rotational infinite order sudden (VCC-IOS) approximation [15]. Calculation of vibrational de-excitation rate coefficients of SO from the first two vibrational levels were reported.

Full-dimensional quantum CC theory has been developed for diatom-diatom scattering [16,17] and successfully used in the rovibrational collisions of diatom-diatom systems in full-dimensionality [18–25]. Very recently Yang et al. [26] reported a full-dimensional quantum calculation of scattering between HF molecules. Coupled-states approximation calculations in 5D and 6D have also been performed for vibrational excitations of diatom-diatom scattering [27–29]. Here we report the first full-dimensional interaction PES and the first vibrational inelastic scattering calculations for the SO(X)-H_2 system. The paper is organized as follows. In Section 2 we briefly describe the theoretical methods for the PES and scattering calculations. The results in terms of inelastic cross sections and rate coefficients are presented in Section 3. Astrophysical applications are discussed in Section 4. Section 5 summarizes the work and presents an outlook on future studies.

2. Theoretical methods

2.1. Potential energy surface computation and fit

We calculated the full-dimensional interaction potential of SO ($X^3\Sigma^-$)-H_2 and described it by 6D Jacobi coordinates as shown in Fig. 1. The resulting PES is a function of (R, r_1, r_2, θ_1, θ_2, ϕ), Where R is the distance between the centers of mass of SO and H_2, and r_1 and r_2 are the bond lengths describing the vibration of SO and H_2, respectively. The angles θ_1 and θ_2, respectively, are the angles between $\vec{r_1}$ and $\vec{R}$ and $\vec{r_2}$ and $\vec{R}$, and ϕ is the out-of-plane dihedral angle.

The ab initio PES computation was performed using the explicitly correlated coupled-cluster (RHF-UCCSD(T)-F12b) method [30,31] with the MOLPRO suite of computational chemistry codes [32,33]. All the calculations employed aug-cc-pwCVQZ (for S and O atoms) and aug-cc-pVQZ (for H atom) orbital basis sets [34–36], and the corresponding MP2FIT auxiliary bases for density fitting and the aug-cc-pwCVQZ-RI auxiliary bases [37,38] for the resolutions of the identify and density-fitted Fock matrices for all orbital bases. No scaled triples correction was used in the CCSD(T)-F12 calculation. The interaction PES was corrected for basis set superposition error (BSSE) [39] using the counter-poise (CP) [40] method. Benchmark calculations at this CCSD (T)-F12 level were carried out on selected molecular configurations and results were compared with those from the conventional CCSD(T) method using aug-cc-pV5Z. The CP corrected interaction energy agrees closely with those derived from CCSD(T)/aug-cc-pV5Z. In the PES

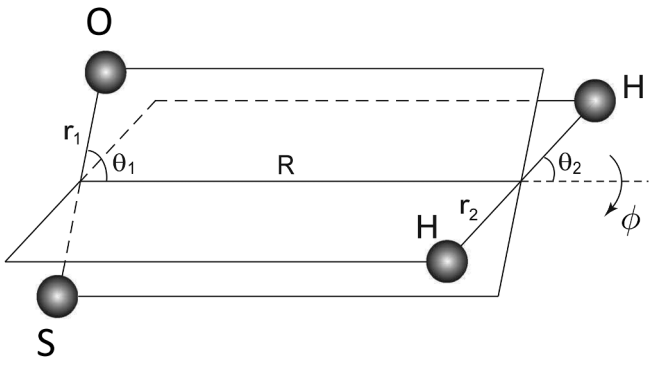

Fig. 1. The six-dimensional Jacobi coordinates for the SO-H_2 system.

calculation R was chosen between 5.8 and 24.0 a_0 and the bond distances are confined to $2.45 \leqslant r_1 \leqslant 3.35$ a_0 and $1.05 \leqslant r_2 \leqslant 2.27$ a_0, where $a_0 = 0.529\times 10^{-10}$ m is the Bohr radius.

The 6D SO-H_2 interaction potential, referred to as VSOH2, was fitted using a two-component method to combine a fit to the full ab initio data set (denoted $V_{\rm I}$) and a fit to the long-range data (denoted $V_{\rm II}$) and is given by

$$V = (1 - s)V_{\rm I} + sV_{\rm II}. \tag{1}$$

The switching function s is given by

$$s = \begin{cases} 0 & (R < R_i) \\ 10b^3 - 15b^4 + 6b^5 & (R_i < R < R_f), \\ 1 & (R > R_f) \end{cases} \tag{2}$$

where $b = (R - R_i)/(R_f - R_i)$, $R_i = 9.0$ a_0 and $R_f = 12.0$ a_0 are the lower and upper bound of the switching region, respectively. Both $V_{\rm I}$ and $V_{\rm II}$ are expanded in the form

$$V_{\rm I,II}(y_1 \cdots y_6) = \sum_{n_1 \cdots n_6} C_{n_1 \cdots n_6} y_1^{n_1} y_6^{n_6} (y_2^{n_2} y_3^{n_3} y_4^{n_4} y_5^{n_5} + y_2^{n_3} y_3^{n_2} y_4^{n_5} y_5^{n_4}) \tag{3}$$

and are fit in 6D using a permutationally invariant polynomial method [41,42], where $y_i = \exp(-d_i/p)$ are Morse-type variables and p is a user-specified parameter with $p = 2.0$ a_0 for $V_{\rm I}$ and $p = 7.0$ a_0 for $V_{\rm II}$. The parameters d_i are the internuclear distances between two atoms and defined as $d_1 = d_{\rm SO}$, $d_2 = d_{\rm SH}$, $d_3 = d_{\rm SH}$, $d_4 = d_{\rm OH}$, $d_5 = d_{\rm OH}$ and $d_6 = d_{\rm HH}$. The powers $n_1, \cdots, n_6$ satisfy $n_1 + \cdots + n_6 \leqslant 7$ and $n_2 + n_3 + n_4 + n_5 \neq 0$. The interaction potential is guaranteed to approach zero when SO and H_2 are infinitely far apart for all r_1 and r_2. The total number of fitted linear coefficients $C_{n_1 \cdots n_6}$ is 882, and these coefficients were determined via linear least-squares fitting using the software MSA [43]. The root mean square (RMS) error in the long range fit $V_{\rm II}$ is 0.062 cm^{-1}, for $V_{\rm I}$ the RMS error is 14.20 cm^{-1}.

The R dependence of VSOH2 PES is shown in Fig. 2 for (θ_1, θ_2, ϕ) = (0°, 0°, 0°), (180°, 0°, 0°), (180°, 90°, 0°), and (90°, 90°, 90°). It is shown that VSOH2 has a depth of -157.58 cm^{-1} at the collinear structure with the O atom towards H_2 and $R = 7.72$ a_0. In Fig. 3 we presented cuts of the SO-H_2 interaction PES as a function of R for $\theta_1 = 0°, 90°, 180°$ for the geometries of H_2 along the z, x, and y axes of the Cartesian coordinates and SO placed along the Oz axis. The bond separations are $r_1 = 2.80$ a_0 and $r_2 = 1.45$ a_0. The comparison between the cuts of VSOH2 and that of the 4D PES of Lique et al. [12] exhibit good agreement. Fig. 4 displays a two-dimensional contour plot of the VSOH2 PES in θ_1 and θ_2 space for $R = 7.70$ a_0, $r_1 = 2.80$ a_0, $r_2 = 1.45$

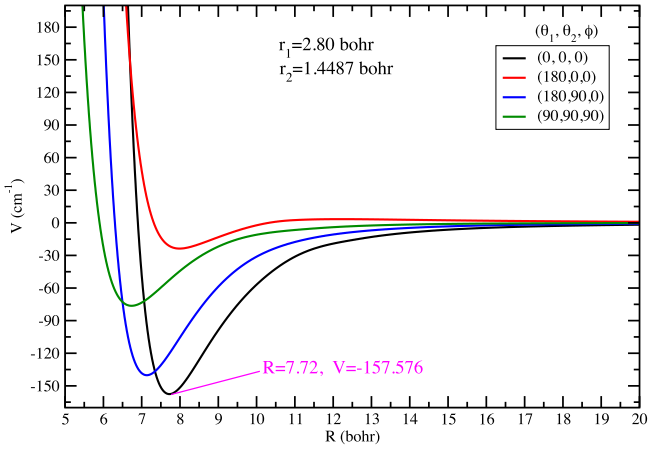

Fig. 2. The R dependence of the SO-H_2 interaction potential, VSOH2 for (θ_1, θ_2, ϕ)= (0°, 0°, 0°), (180°, 0°, 0°), (180°, 90°, 0°), and (90°, 90°, 90°). The bond lengths of SO and H_2 are fixed at the equilibrium value and the vibrationally averaged value in the vibrational ground state, respectively.

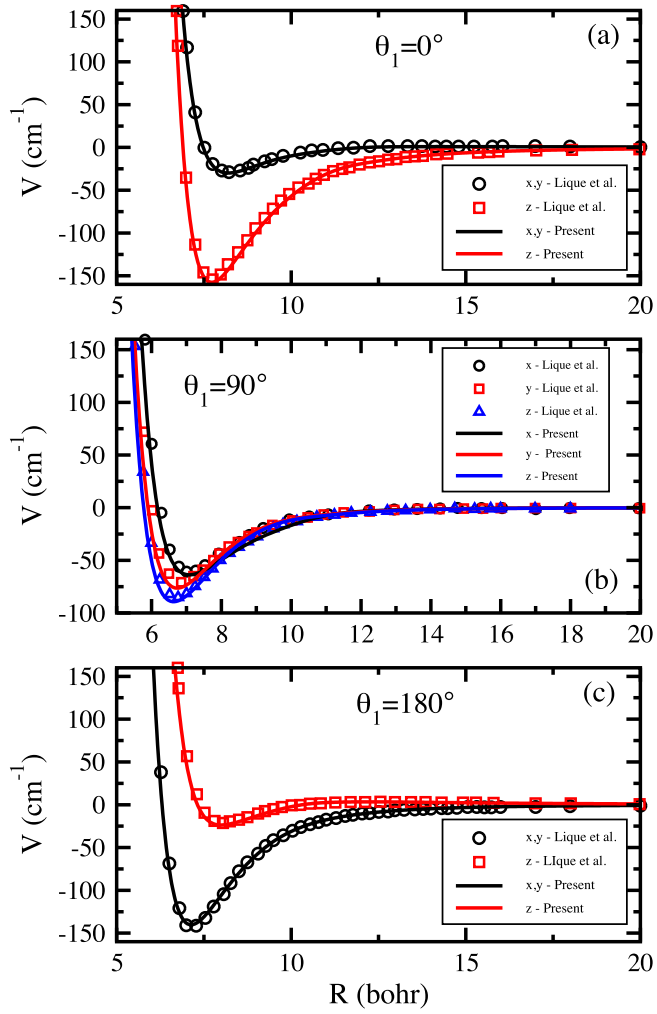

Fig. 3. Cuts of the SO-H_2 interaction PESs as a function of R. Lines are for the present VSOH2 PES and symbols are for the 4D PES of Lique et al. [12]. See text for further details.

a_0, and $\phi = 0°$. In Table 1 the global minimums of 4D PESs of VSOH2 and Lique et al. [12] are compared.

2.2. Scattering calculation

We used the TwoBC code [44] to perform the full-dimensional CC

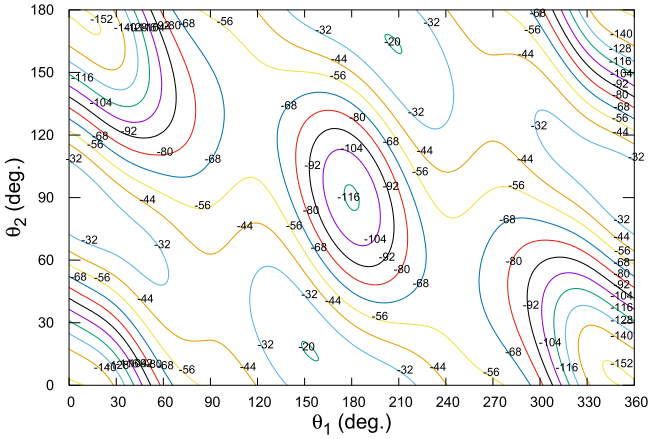

Fig. 4. Contour plots of the potential VSOH2 as a function of θ_1 and θ_2 for $r_1 = 2.80\ a_0$, $r_2 = 1.40\ a_0$, $R = 7.70\ a_0$, and $\phi = 0°$.

Table 1
Global minimum of SO-H_2 PESs.

PES	Well depth (cm^{-1})	R (a_0)	θ_1	θ_2	ϕ	r_1 (a_0)[c]	r_2 (a_0)[c]
VSOH2	−152.44	7.72	0°	0°	0°	1.40	2.80
VSOH2	−157.58	7.72	0°	0°	0°	1.45	2.80
Lique et al.[a]	−154.27[b]	7.75[b]	0°	0°	0°	1.45	2.80

[a] Lique et al. [12]. [b] Digitized from Fig. 1 of Lique et al. [c] H_2 equilibrium bond length is 1.4011 a_0 and vibrational averaged bond length in ground vibrational state is 1.4487 a_0. Equilibrium bond length of SO is 2.80 a_0.

scattering calculations for SO($X^3\Sigma^-$) due to ortho- and para-H_2 collisions. The spin-rotation coupling is ignored in the scattering calculations. The reader is referred to Refs. [21,45] for the methodology of the full-dimensional diatom-diatom rovibrational scattering. In the scattering calculations the angular dependence of the interaction potential VSOH2, $V(R, r_1, r_2, \theta_1, \theta_2, \phi)$, is expanded in the form [46],

$$V(R, r_1, r_2, \theta_1, \theta_2, \phi) = \sum_{\lambda_1\lambda_2\lambda_{12}} A_{\lambda_1\lambda_2\lambda_{12}}(r_1, r_2, R) \times Y_{\lambda_1\lambda_2\lambda_{12}}(\hat{r}_1, \hat{r}_2, \hat{R}), \tag{4}$$

where $Y_{\lambda_1\lambda_2\lambda_{12}}$ is a bi-spherical harmonic function [24]. Terms $0 \leqslant \lambda_1 \leqslant 8$ and $0 \leqslant \lambda_2 \leqslant 4$ are used to expand the interaction potential. Due to the symmetry of H_2, only even λ_2 terms are retained.

We use (v_1, j_1) and (v_2, j_2) to describe the rovibrational states of SO and H_2, respectively, where v_i and j_i $(i = 1, 2)$ are the vibrational and rotational quantum numbers. For combination of rovibrational states for SO $(v_1 j_1)$ and H_2 $(v_2 j_2)$, a combined molecular state (CMS) [45] notation, $\alpha = (v_1 j_1 v_2 j_2)$ is used. The coupled scattering equations are solved using the CC method as implemented in TwoBC. The state-to-state rovibrational excitation cross section can be computed as a function of the collision energy E_c,

$$\sigma_{\alpha\to\alpha'}(E_c) = \frac{\pi}{(2j_1+1)(2j_2+1)k^2} \times \sum_{j_{12}j'_{12}ll'J_{\mathrm{tot}}} (2J+1) \left| \delta_{\alpha,\alpha'} - S^{J_{\mathrm{tot}}}_{\alpha j_{12} l, \alpha' j'_{12} l'}(E_c) \right|^2, \tag{5}$$

where $S^{J_{\mathrm{tot}}}_{\alpha l, \alpha' l'}(E_c)$ is the scattering S-matrix, l is the orbital angular momentum quantum number, and the quantum number J denotes the total angular momentum, $\vec{J} = \vec{l} + \vec{j}_{12}$, with $\vec{j}_{12} = \vec{j}_1 + \vec{j}_2$. The wave vector $k = \sqrt{2\mu E_c/\hbar^2}$.

The total quenching cross section of SO from initial CMS $(v_1 j_1 v_2 j_2) \to (v'_1 v'_2 j'_2)$ can be calculated by summing the state-to-state cross sections over the j'_1 states of SO in state v'_1,

$$\sigma_{v_1 j_1 v_2 j_2 \to v'_1 v'_2 j'_2}(E_c) = \sum_{j'_1} \sigma_{v_1 j_1 v_2 j_2 \to v'^1 j'^1 v'^2 j'^2}(E_c). \tag{6}$$

The state-to-state rate coefficients at temperatures T are obtained by integrating the state-to-state cross section $\sigma_{v_1 j_1 v_2 j_2 \to v'^1 j'^1 v'^2 j'^2}$ over collision energy (E_c),

$$k_{\alpha\to\alpha'}(T) = \left(\frac{8}{\pi\mu\beta}\right)^{1/2} \beta^2 \times \int_0^\infty E_c \sigma_{\alpha\to\alpha'}(E_c) \times \exp(-\beta E_c) dE_c, \tag{7}$$

where μ is the reduced mass of the SO-H_2 system, $\beta = (k_B T)^{-1}$, and k_B is Boltzmann's constant.

In the full-dimensional quantum scattering calculations we use the log-derivative matrix propagation method of Johnson [47] to propagate the CC equations from $R = 4.5\ a_0$ to $24\ a_0$. In Table 2 the numbers of Gauss-Legendre quadrature points in θ_1 and θ_2, Chebyshev quadrature points in ϕ, and Gauss-Hermite quadrature points N_{r_1}, N_{r_2} are listed. The monomer potentials of Qian et al. [48] and Schwenke [49] are applied to calculate the rovibrational levels of SO and H_2, respectively.

Table 2
TwoBC parameters used in the scattering calculations.

Basis set		λ_1	λ_2	$N_{\theta_1}(N_{\theta_2})$	N_ϕ	$N_{r_1}(N_{r_2})$	$JTOT_{max}$ [b]
6D Rotation							
para-H_2-SO	$j_1^{max} = 30, j_2 = 0, 2$	8	4	12	8	18	160
ortho-H_2-SO	$j_1^{max} = 30, j_2 = 1, 3$	8	4	12	8	18	160
6D Rovibration							
para-H_2-SO	[(0,35;1,20)(0,2)] [a]	8	4	12	8	18	160
ortho-H_2-SO	[(0,35;1,20)(0,3)] [a]	8	4	12	8	18	160

[a] Basis set $[(v_1 = 0, j_{v_1=0}^{max}; v_1 = 1, j_{v_1=1}^{max})(v_2 = 0, j_{v_2=0}^{max})]$ is presented by the maximum rotational quantum number $j_{v_1}^{max}$ and $j_{v_2}^{max}$ included in each relevant vibrational level v_1 and v_2 for SO and H_2, respectively. [b] Maximum value of total angular momentum quantum number J used in scattering calculations.

3. Results and discussion

3.1. Pure rotational de-excitation

We first use the 6D VSOH2 PES to calculate rotational de-excitation cross sections of SO (j_1) in collision with H_2 (j_2), $j_2 = 0$ and 1 for para-H_2 and ortho-H_2, respectively. Both SO and H_2 are in their ground vibrational states, i.e, rotational transitions are $(0\ j_1\ 0\ j_2) \rightarrow (0\ j_1'\ 0\ j_2')$. Full-dimensional scattering calculations were carried out for the initial rotational states of SO $j_1 = 1 - 5$ and collision energies from 1 to 3000 cm^{-1}. We include sufficient number of partial waves in the scattering calculations to ensure the convergence of the state-to-state integral cross sections. For the rotational basis included in the calculations, we performed convergence test with respect to para-H_2 basis including $j_2 = 0$, 2, and 4. Well converged cross sections were obtained for the para-H_2 basis with inclusion of $j_2 = 0$ and 2. In Table 2 we provide the input TwoBC parameters used in the scattering calculations. From previous diatom-diatom collision studies, we find that $R_{max} = 24$ a_0 is sufficient to converge the cross section, for collision energies greater than 1 cm^{-1}.

Fig. 5 shows the rotational cross sections of SO from initial state $j_1 = 4$ and 6 in collisions with ortho-H_2 ($j_2 = 1$) and para-H_2 ($j_2 = 0$) for quenching transitions $j_1 \rightarrow j_1'$. We can see that the quenching cross sections for para-H_2 collider display richer resonance structures than the cross section for ortho-H_2. The resonances occur at collision energies below about 60 cm^{-1} and are due to the van der Waals well of the PES. In the whole energy range considered, the rotational quenching cross sections are dominated by $\Delta j_1 = j_1' - j_1 = -1$ transition and the $j_1' \rightarrow 0$ transition is the smallest for both initial states $j_1 = 4$ and 6. For SO in collision with ortho-H_2, following the energy-gap law, the state-to-state cross section increases with increasing j_1'. One exception is that the cross sections for transitions $j_1 = 6 \rightarrow 2$ and $j_1 = 6 \rightarrow 1$ merge together above 300 cm^{-1}. For collisions with para-H_2 and $j_1 = 4$, the trend found for ortho-H_2 cross sections is generally followed except for collision energies below 40 cm^{-1}, where the resonances mix the magnitude of the cross sections of the $j_1 = 4 \rightarrow 2$ and $j_1 = 4 \rightarrow 1$ transitions. For quenching from $j_1 = 6$, however, the general trend is not clear, and the energy-gap law behavior can only be observed for collision energies above ~ 500 cm^{-1}.

Fig. 6 presents the total rotational quenching cross sections of SO from initial states $j_1 = 1 - 10$ for colliders ortho-H_2 ($j_2 = 1$) and para-H_2 ($j_2 = 0$). We can see that for both ortho- and para-H_2 the resonances shown in the state-to-state quenching cross sections can also be observed in the total quenching cross sections, particularly in the initial $j_1 = 1$ state. These resonances disappear for energies greater than ~80 cm^{-1}. Moreover, the total quenching cross sections of ortho-H_2 show more resonance structure than para-H_2. For ortho-H_2, generally the total rotational quenching cross sections increase with increasing initial j_1 and the cross sections decrease with increasing collision energy over the whole energy range. While for para-H_2, due to the resonances at collision energy below ~30 cm^{-1}, no obvious trend can be observed for the cross sections of $j_1 > 2$. While for collision energy above 30 cm^{-1}, the total quenching cross sections show similar trends as found for ortho-H_2.

We show in Fig. 7(a)–(d) the rate coefficients as a function of temperature for rotational quenching of SO from $j_1 = 3$ and 5 induced by ortho- and para-H_2 collisions, respectively. Over the whole temperature range of 5 to 600 K, the $\Delta j_1 = -1$ transition is dominant for all initial states. For collider ortho-H_2, both $j_1 = 3$ and 5 show the same trend that the rate coefficients increase with increasing j_1' over the whole temperature range. Initial $j_1 = 3$ of SO with collider para-H_2 show similar trends. However, $j_1 = 5$ with para-H_2 does not show such an obvious trend. Due to the different resonance structures in the state-to-state cross sections, the rate coefficients show different behaviors at temperatures below 100 K. It also can be noted that except for the transition $j_1 = 3 \rightarrow 0$, the rate coefficients of nearly all transitions increase slowly with increasing temperature for temperature above 100 K.

Lique et al. [12] reported collisional rate coefficients between the fine-structure levels of SO due to para-H_2 collisions, but used a 2-dimensional PES obtained by averaging the 4D PES over θ_2 and ϕ. The well depth of the averaged 2D PES is -93.81 cm^{-1} compared to the well depth of ~ -155 cm^{-1} for their 4D PES and -157.58 cm^{-1} obtained for VSOH2. In their scattering calculations, para-H_2 was treated as a structureless target. To compare our rotational rate coefficients $r_{j_1 \rightarrow j_1'}$ with the fine-structure rate coefficients $r_{j_1 F \rightarrow j_1' F'}$ of Lique et al. [12], the following statistical averaging relation was adopted,

$$r_{j_1 \rightarrow j_1'} = \frac{\sum_{FF'} r_{j_1 F \rightarrow j_1' F'} (2F + 1)(2F' + 1)}{\sum_{FF'} (2F + 1)(2F' + 1)}. \quad (8)$$

In Fig. 8 the state-to-state rate coefficients for deexcitation from SO initial state $j_1 = 5$ and 10 for $|\Delta j_1| = |j_1' - j_1| = 1$–5 are compared for para-H_2 collisions. For $j_1 = 5$, except the transition to $j_1' = 0$ which shows very good agreement between our rate coefficient and the results of Lique et al., the rate coefficients for other transitions differ by a factor of 5–10 with no clear trend. On the other hand, from Fig. 8 (b) we can see that reasonable agreement is shown between our rate coefficients and those of Lique et al. This suggests that for relatively high j_1, the fine-structure changing transitions approach a statistical equilibrium description.

3.2. Vibrational quenching

Our main focus of this paper is to report the vibrational quenching cross sections and rate coefficient of SO in collisions with ortho- and para-H_2. The rovibrational scattering calculations were carried out using the TwoBC code with the full-dimensional close-coupling theory. We calculated the state-to-state quenching cross sections for the rovibrational transitions $SO(v_1 = 1, j_1) + H_2(v_2 = 0, j_2) \rightarrow SO(v_1' = 0, j_1') + H_2(v_2' = 0, j_2')$, i.e., $(1\ j_1\ 0\ j_2) \rightarrow (0\ j_1'\ 0\ j_2')$. In the calculations, initial rotational states $j_1 = 0$–5 were selected and final rotational levels in v_1' are $j_1' = 0, 1, 2, \cdots, 35$. Only the pure rotational excitations of H_2 within its ground vibrational $v_2 = 0$ state were considered. The initial and final rotational levels of H_2 are $j_2 = 0$ and $j_2' = 0$ and 2 for para-H_2, while for ortho-H_2, $j_2 = 1$ and $j_2' = 1$ and 3. We provide in Table 2 the basis sets applied in the scattering calculations. The vibrational quenching cross sections are reported for collision energies between 1 and 3000 cm^{-1}.

Examples of the state-to-state rovibrational quenching cross sections from initial CMS (1000) and (1001) into selected final rotational states in $v_1' = 0$, $j_1' = 0$, 5, 10, 15, 20, 25, 30, and 35 are given in Fig. 9. Meanwhile, the total vibrational quenching cross sections are also displayed for colliders para-H_2 and ortho-H_2, respectively. These cross sections correspond to H_2 elastic transitions, i.e., $j_2 = 0 \rightarrow j_2' = 0$ for para-H_2 and $j_2 = 1 \rightarrow j_2' = 1$ for ortho-H_2. We can see from Fig. 9 that a

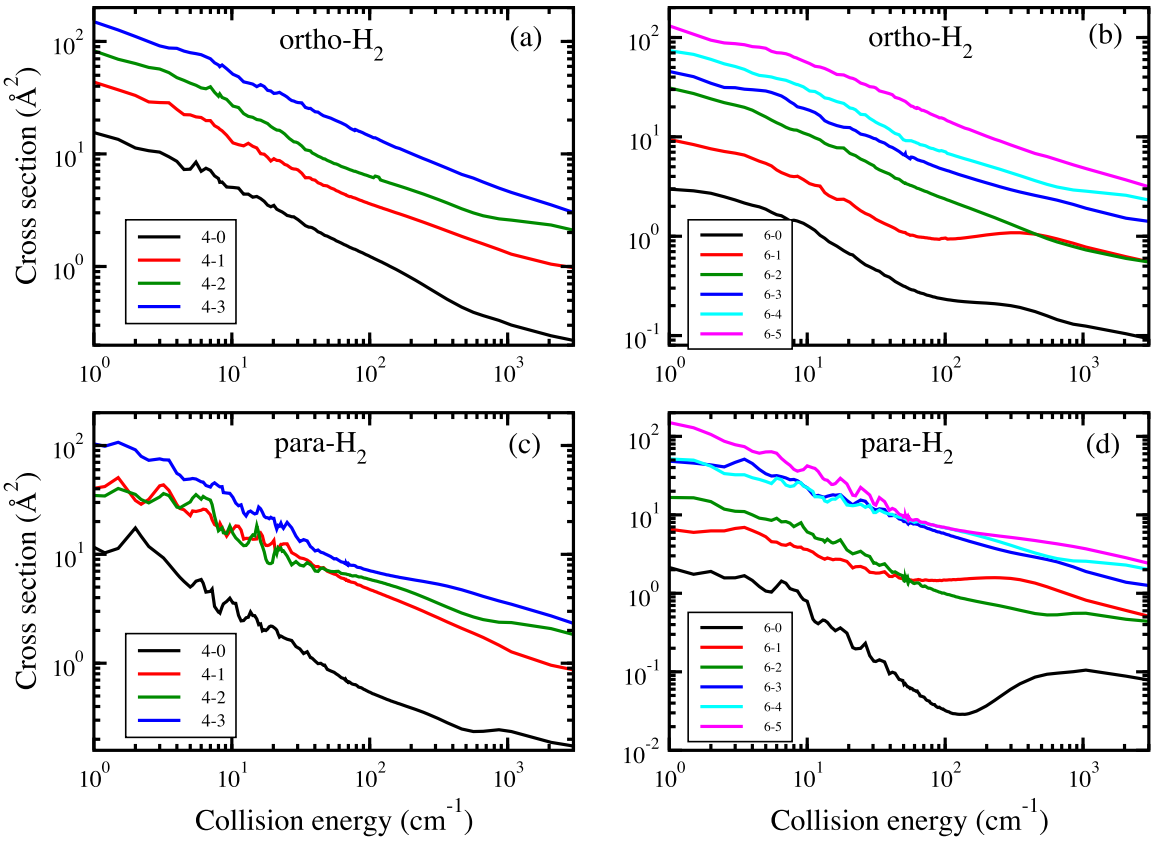

Fig. 5. Rotational state-to-state de-excitation cross sections for SO(j_1) + H_2(j_2) → SO (j_1') + H_2(j_2'), j_1 = 4 and 6, $j_1' < j_1$. (a) and (b): SO in collision with ortho-H_2, $j_2 = j_2' = 1$; (c) and (d): SO in collision with para-H_2, $j_2 = j_2' = 0$.

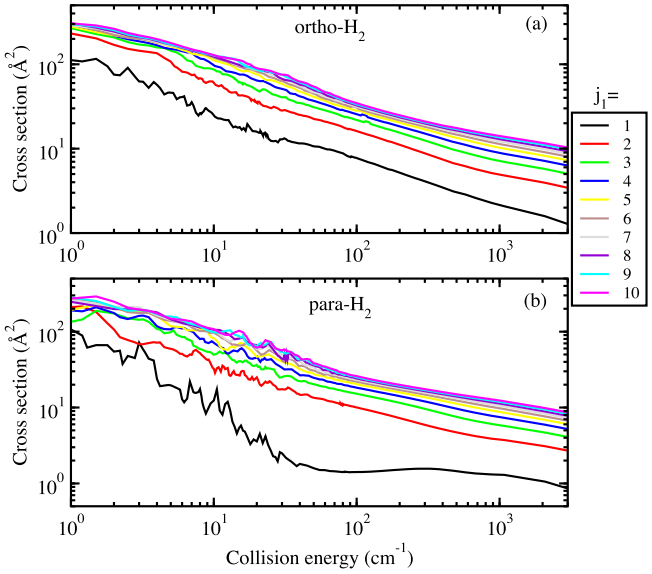

Fig. 6. Total rotational de-excitation cross sections for SO(j_1) from initial states j_1 = 1, 2, ⋯, 10 (from bottom to top at high energy). (a) SO in collision with ortho-H_2, $j_2 = j_2' = 1$; (b) SO in collision with para-H_2, $j_2 = j_2' = 0$.

large number of resonances are observed in the cross sections at low collision energies for both para-H_2 and ortho-H_2 colliders and the resonances persist to higher collision energies up to ~200 cm^{-1} with increasing final j_1'. In addition, one can note that the state-to-state and total quenching cross sections increase with collision energy for energies above ~ 200 cm^{-1}. In general, the state-to-state cross sections for $j_1' \leqslant 20$ display similar resonance structures and energy dependence. The quenching cross section values for $j_1' = 20$, 25 and 30 range from two to ten orders of magnitude smaller than the transitions for $j_1' < 20$ for collision energies below 300 cm^{-1} for both para- and ortho-H_2. However, for collision energies above 300 cm^{-1}, these cross sections increase rapidly with collision energy ultimately merging together at an energy of 3000 cm^{-1}. Finally, it should be noted that the vibrational quenching cross sections are several orders of magnitude smaller than the pure rotational quenching cross sections. Because vibrational quenching is very slow, the scattering SO-H_2 complex may be trapped in excited vibrational states with long lifetimes [50,51]. This appears to result in a more complicated resonance structure for vibrational quenching cross sections (compare Figs. 5 and 9).

Fig. 10(a) and (b) compare the final rotational distribution of SO in $v_1' = 0$ for quenching from initial CMSs (1000) and (1001), respectively, at collision energy of 1.0 cm^{-1}. We can see that the final rotational distributions are broad expanding from 0 to 22 for para-H_2 and to 25 for ortho-H_2; here the transitions with cross section smaller than 10^{-5} $Å^2$ are not shown. Generally, the distribution is dominated by final $j_1' = 5 - 8$ for para-H_2 and $j_1' = 4$, 5, 11, and 12 for ortho-H_2. The distributions fall off quickly above $j_1' = 20$. While between $j_1' = 11$ and 18 the distribution shows some fluctuation, but only for para-H_2.

We calculated the total vibrational quenching cross section of SO from $v_1 = 1$ to $v_1' = 0$ using Eq. (6). These total quenching cross section have been obtained for elastic and inelastic rotational transitions in H_2. Fig. 11(a) and (b) show the collision energy dependence of the total $v_1 = 1 \rightarrow v_1' = 0$ quenching cross section of SO in collision with para-H_2 from CMSs (1000) and (1300). The results are presented for elastic ($j_2 = 0 \rightarrow j_2' = 0$) and inelastic ($j_2 = 0 \rightarrow j_2' = 2$) transitions of H_2. We can first observe the resonances at collision energies below 50 cm^{-1}. While the total vibrational cross sections for initial CMSs (1000) and (1300) display similar energy dependencies, the cross sections for $j_2 = 0 \rightarrow 2$ transition are larger than that for $j_2 = 0 \rightarrow 0$ transition at

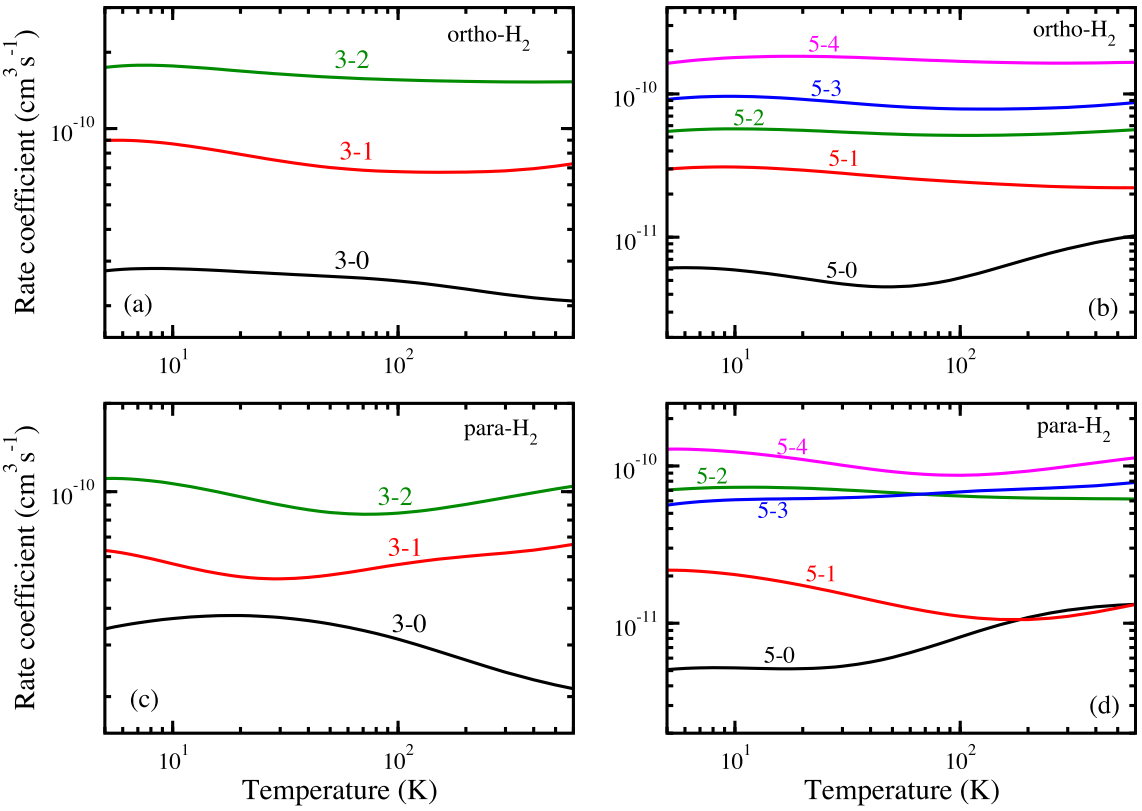

Fig. 7. Rotational state-to-state de-excitation rate coefficients from initial $j_1 = 3$ and 5 of SO in collision with (a) and (b) ortho-H_2($j_2 = 1$), and (c) and (d) para-H_2($j_2 = 0$).

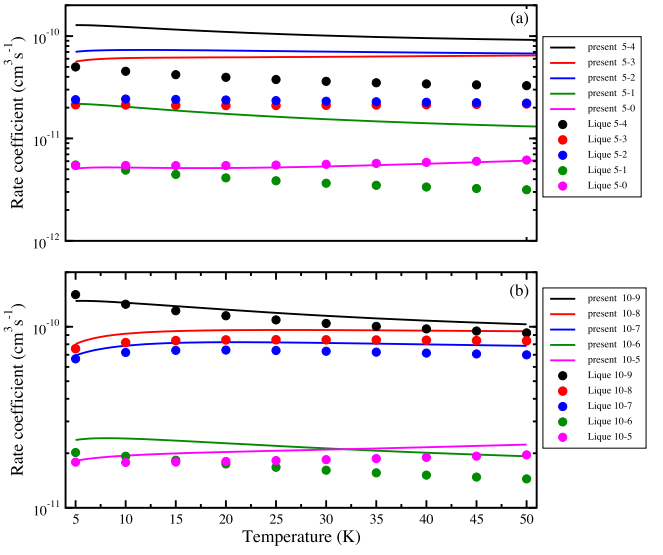

Fig. 8. Rotational state-to-state de-excitation rate coefficients compared with Lique et al. [12] for SO in collision with para-H_2($j_2 = 0$) from initial state (a) $j_1 = 5$ and (b) $j_1 = 10$. The results from Lique et al. have been averaged over fine-structure levels.

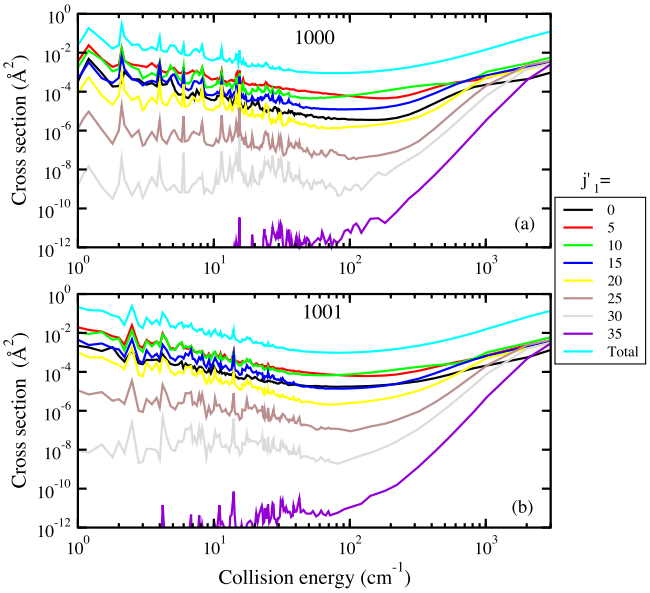

Fig. 9. Vibrational state-to-state and total quenching cross section for transitions SO($v_1 = 1$, $j_1 = 0$) + H_2(j_2) → SO ($v_1' = 0$, j_1') + H_2(j_2), $j_1' = 0$, 5, 10, 15, 20, 25, 30, and 35. (a) para-H_2($j_2 = 0$) and initial state (1000), (b) ortho-H_2($j_2 = 1$) and initial state (1001).

energies smaller than 400 cm^{-1}. For high energies, the H_2 elastic transition becomes the larger one and the difference increases with increasing collision energy. For ortho-H_2 collider and initial CMSs (1001) and (1301), similar to the case of para-H_2, Fig. 11(c) and (d) show that the total quenching cross sections for inelastic ($j_2 = 1 \rightarrow j_2' = 3$) transition are about a factor of two larger than its elastic counterpart for energies below ~200 cm^{-1}. For energies greater than ~200 cm^{-1}, the cross section for H_2 $j_2 = 1 \rightarrow 1$ transition becomes increasingly dominant. However, the inelastic cross sections to $j_2' = 2$ or 3 may not be fully-converged as they are the top states in our H_2 bases.

The state-to-state and total vibrational quenching rate coefficients of SO($v_1 = 1$, j_1) due to collisions with ortho-H_2($j_2 = 1$) and para-H_2($j_2 = 0$) were also calculated for $j_1 = 0 - 5$ and $j_1' = 0, 1, 2, \cdots, 35$. Both H_2 elastic and inelastic transitions were considered. Fig. 12(a) and

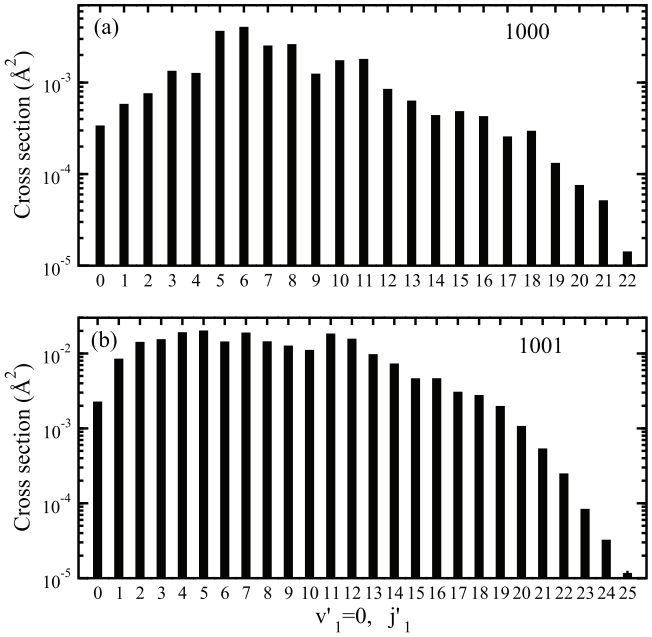

Fig. 10. Distribution of final rotational states in $v_1' = 0$ for vibrational quenching of SO($v_1 = 1$, $j_1 = 0$) + $H_2(j_2) \rightarrow$ SO ($v_1' = 0$, j_1') + $H_2(j_2)$, $j_1' = 0, 1, 2, \cdots, 25$ at 1 cm^{-1}. (a) para-H_2($j_2 = 0$), (b) ortho-H_2($j_2 = 1$).

(c) show the total vibrational quenching cross sections and rate coefficient for para-H_2 and ortho-H_2 and $j_1 = 0 - 5$. For the total quenching cross sections, we can see that numerous resonances are observed at energies below ~30 cm^{-1}, particularly for $j_1 = 0$, 1, and 2, while the resonances are suppressed with increasing j_1. Also, in all cases, the cross sections show qualitatively the same energy dependence. From 100 cm^{-1} the cross sections increase rapidly with energy. For either para-H_2 or ortho-H_2 the total quenching cross sections from all initial rotational levels in $v_1 = 1$ have very similar magnitude. The total vibrational quenching rate coefficients from $j_1 = 0$–5 are plotted in Fig. 12(b) and (d). Due to the different resonance structures in the total vibrational quenching cross sections, the total vibrational quenching rate coefficients show different behavior, but generally, they decrease initially and then increase with temperature.

Finally, Fig. 13 compares the total vibrational quenching rate coefficients of SO-H_2 for CMS (1000) to ($v_1' = 0$) and $j_2' = 0$, and CMS (1001) to ($v_1' = 0$) and $j_2' = 1$ with that of CO-H_2 (Ref.[21]), SiO-H_2 (Ref.[24]), and CS-H_2 (Ref.[25]). A similar comparison of total vibrational rate coefficients was also made in Ref.[25]. Fig. 13 shows that the rate coefficients generally increase with the well-depth of the interaction potential: 93 (CO-H_2), 162 (CS-H_2), 279 (SO-H_2), and 292 cm^{-1} (SiO-H_2).

4. Astrophysical applications

As discussed in the Introduction, a quantitative modeling of astrophysical phenomena from submillimetre and infrared observations requires detailed knowledge of molecular collisional rate coefficients over a wide range of temperatures and levels for systems of astrophysical interest. In spite of the progress in experiments and computation to provide molecular collisional data, there is still a significant lack of collisional rate coefficients for astrophysical modeling, especially for scattering systems of four and more atoms and involving vibrational excitation.

Sulfur monoxide is commonly detected in cold dense regions with abundances about 10^{-9} [52]. A 3 mm line survey was performed by Agúndez et al. [53] for the optically dark cloud core L483 located in the Aquila Rift star-forming region. SO and its isotopic species were

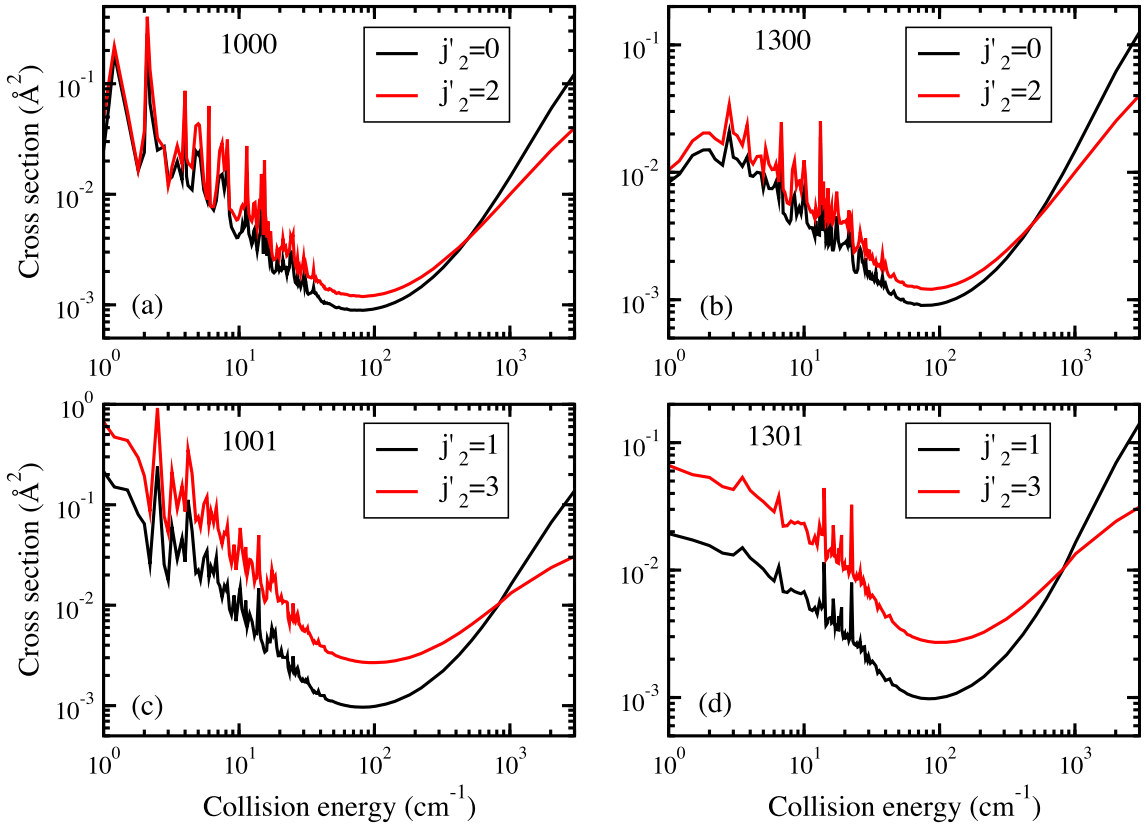

Fig. 11. Total vibrational quenching cross section for transitions SO($v_1 = 1$, j_1) + $H_2(j_2) \rightarrow$ SO ($v_1' = 0$) + $H_2(j_2')$. (a) Initial CMS (1000), $j_2' = 0$ and 2; (b) initial CMS (1300), $j_2' = 0$ and 2; (c) initial CMS (1001), $j_2' = 1$ and 3; (d) initial CMS (1301), $j_2' = 1$ and 3.

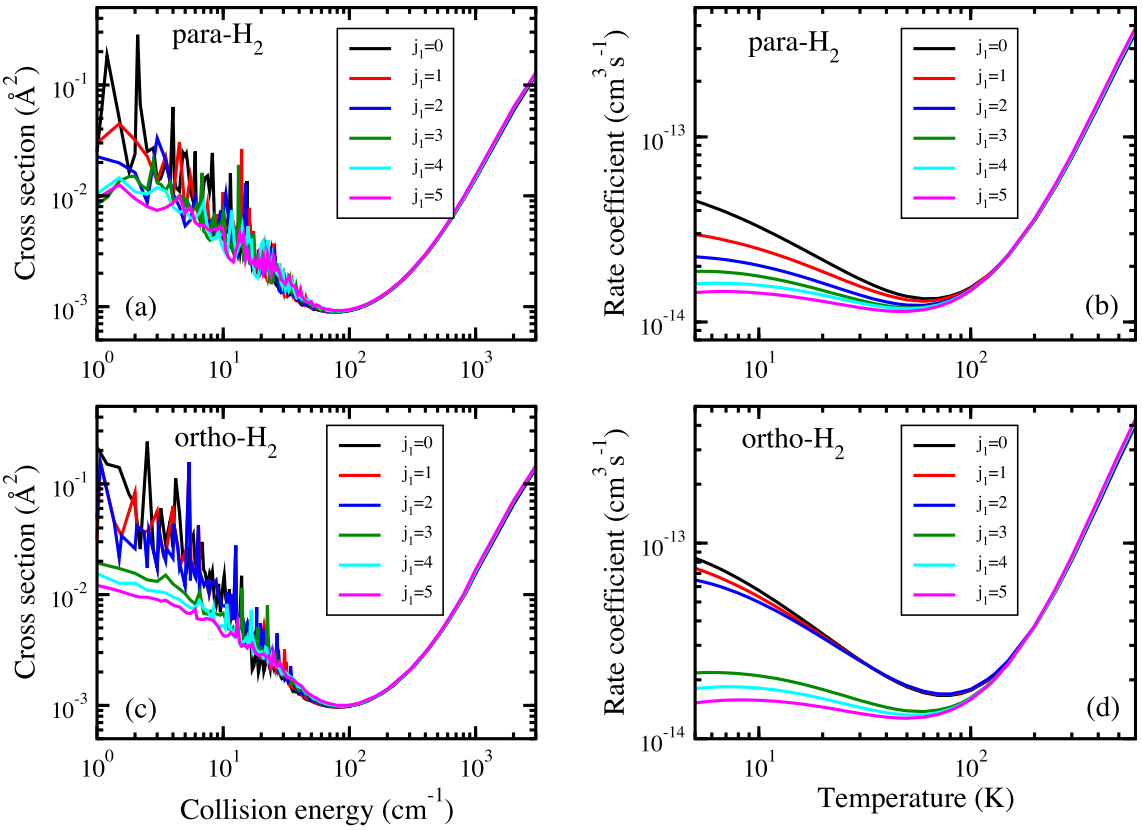

Fig. 12. Total cross sections and rate coefficients for the vibrational quenching of SO from CMSs $(1j_10j_2)$. j_1 = 1, 2, ⋯, 5 and $j_2 = j_2'$. Upper panels are for para-H_2, lower panels are for ortho-H_2.

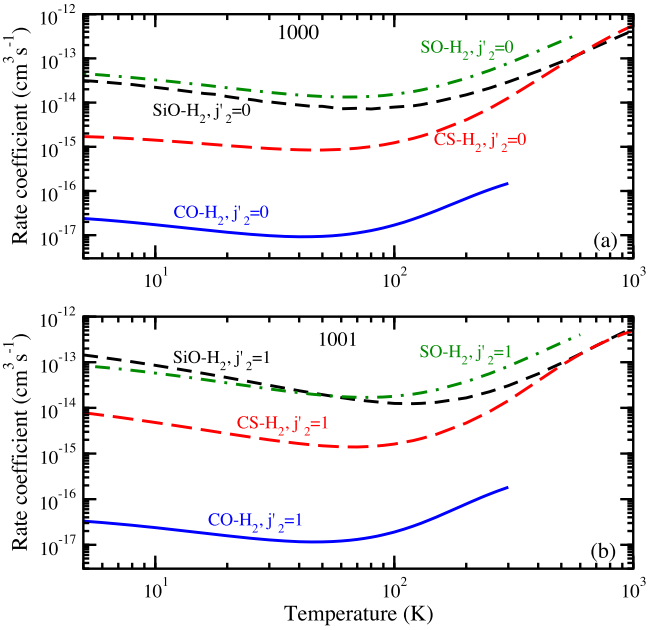

Fig. 13. Total rate coefficients for the vibrational quenching of SO compared to the same transitions for CO from Ref.[21], SiO from Ref.[24], and CS from Ref. [25]. (a) from (1000) to $v_1' = 0$ + para-$H_2(v_2' = 0, j_2' = 0)$. (b) from (1001) to $v_1' = 0$ + ortho-$H_2(v_2' = 0, j_2' = 1)$.

detected. Loison et al. [54] reported a gas-grain model for sulfur and oxygen isotopic fractionation in cold cores. The $S^{16}O/S^{18}O$ ratio was predicted and shown to be used as a sensitive chemical proxy for matter evolution in dense molecular clouds. Spectroscopic constants were measured by Lattanzi et al. [55] for SO and its isotopologues. Their measurements were also used in an isotopically invariant fit with pure rotational and ro-vibrational transitions for all of the SO isotopologues. Martin-Drumel et al. [56] measured the spectroscopic characterization of SO and its isotopologues and performed an isotopically invariant fit based on pure rotational and ro-vibrational transitions of all SO isotopologues. Observation of SO towards the transitional disks AB Auriga [57] and DM Tau [58] were reported, and SO was the second S-bearing molecule detected in a protoplanetary disk (PPD) after CS. As predicted by Martin-Drumel et al. [56], their spectroscopic parameters of the ro-vibrational lines with high accuracy could enable the study of SO in the mid-IR using ground-based telescopes, space-based telescopes (Infrared Space Observatory (ISO), Spitzer), and the future observational facilities such as the James Webb Space Telescope (JWST).

Vibrationally excited molecules, which are excited by collision or radiation, can be employed to investigate astrophysical environments with high gas densities and temperatures. SO vibrational bands will be accessible by JWST. In PPDs, SO vibrational lines probe the inner warm regions which are exposed to the UV radiation from the protostar. Our rovibrational cross sections and rate coefficients of SO in collisions with H_2 based on the full-dimensional quantum CC calculation will be able to provide accurate data for future modeling of protostars, the infrared sources, and future FIR and submillimeter observations.

5. Summary

Full-dimensional quantum close-coupling calculations of rotational and vibrational quenching of $SO(X^3\Sigma^-)$ in collisions with H_2 have been carried out on a 6D potential energy surface. The PES was constructed based on high-level electronic structure calculation and a hybrid invariant polynomial fit. State-to-state and total cross sections and rate coefficients for rotational and rovibrational transitions in SO are presented for elastic and inelastic rotational transitions in para- and ortho-

H_2. The state-to-state rotational rate coefficients of SO with para-H_2 are compared with the rigid-rotor approximation calculations of Lique et al. [12] using an averaged 2-dimensional potential surface. We report here for the first time the vibrational quenching cross sections and rate coefficients of SO from $v_1 = 1$, $j_1 = 0$–5. A large number of resonances were observed for both rotational and vibrational quenching transitions at low collision energies. Our computed rate coefficients will be useful for astrophysical modeling. In future work, we will extend our present calculations to higher vibrational ($v_1 > 1$) and rotational states ($j_1 > 5$) of SO and include fine-structure resolution using quantum close-coupling methods and the coupled-states approximation.

CRediT authorship contribution statement

Benhui Yang: Investigation, Writing - original draft. **P. Zhang:** Software, Investigation, Data curation. **C. Qu:** Software, Investigation. **P.C. Stancil:** Conceptualization, Supervision, Writing - review & editing. **J.M. Bowman:** Data curation, Writing - review & editing. **N. Balakrishnan:** Software, Writing - review & editing. **R.C. Forrey:** Writing - review & editing.

Declaration of Competing Interest

The authors declare that they have no known competing financial interests or personal relationships that could have appeared to influence the work reported in this paper.

Acknowledgements

This work was supported by NASA grant NNX16AF09G. Further, work at UNLV was partially supported by NSF Grant No. PHY-1806334, and at Penn State by NSF Grant No. PHY-1806180.

Appendix. Supplementary data

Supplementary data to this article can be found online at https://doi.org/10.1016/j.chemphys.2020.110695. The VSOH2 subroutine can be obtained online. The supplementary data can be used to generate Fig. 2.

References

[1] E. Roueff, F. Lique, Chem. Rev. 113 (2013) 8906–8938.
[2] C.A. Gottlieb, J.A. Ball, Astrophys. J. 184 (1973) L59.
[3] O.E.H. Rydbeck, et al., Astrophys. J. 235 (1980) L171.
[4] G.A. Blake, E.C. Sutton, C.R. Masson, T.G. Phillips, Astrophys. J. 315 (1987) 621.
[5] V. Wakelam, A. Castets, C. Ceccarelli, B. Lefloch, E. Caux, L. Pagani, Astron. Astrophys. 413 (2004) 609.
[6] G.B. Esplugues, et al., Astron. Astrophys. 556 (2013) A143.
[7] F. Herpin, M. Marseille, V. Wakelam, S. Bontemps, D.C. Lis, Astron. Astrophys. 504 (2009) 853.
[8] D.S. Meier, et al., Astrophys. J. 801 (2015) 63.
[9] D.A. Neufeld, B. Godard, M. Gerin, et al., Astron. Astrophys. 577 (2015) A49.
[10] L. Velilla Prieto, C. Sánchez Contreras, J. Cernicharo, et al., Astron. Astrophys. 597 (2017) A25.
[11] S. Green, Astrophys. J. 434 (1994) 188.
[12] F. Lique, M.-L. Senent, A. Spielfiedel, N. Feautrier, J. Chem. Phys. 126 (2007) 164312.
[13] P.J. Knowles, C. Hampel, H.-J. Werner, J. Chem. Phys. 112 (2000) 3106.
[14] D.E. Woon, T.H. Dunning Jr., J. Chem. Phys. 100 (1994) 2975.
[15] F. Lique, A. Spielfiedel, G. Dhont, N. Feautrier, Astron. Astrophys. 458 (2006) 331.
[16] K. Takayanagi, Adv. At. Mol. Phys. 1 (1965) 149–194.
[17] S.K. Pogrebnya, D.C. Clary, Chem. Phys. Lett. 363 (2002) 523–528.
[18] G. Quéméner, N. Balakrishnan, R.V. Krems, Phys. Rev. A 77 (2008) 030704.
[19] S.F. dos Santos, N. Balakrishnan, S. Lepp, G. Quéméner, R.C. Forrey, R.J. Hinde, P.C. Stancil, J. Chem. Phys. 134 (2011) 214303.
[20] S.F. dos Santos, N. Balakrishnan, R.C. Forrey, P.C. Stancil, J. Chem. Phys. 138 (2013) 104302.
[21] B.H. Yang, P. Zhang, X. Wang, P.C. Stancil, J.M. Bowman, N. Balakrishnan, R.C. Forrey, Nat. Commun. 6 (2015) 6629.
[22] B.H. Yang, N. Balakrishnan, P. Zhang, X. Wang, J.M. Bowman, R.C. Forrey, P.C. Stancil, J. Chem. Phys. 145 (2016) 034308.
[23] B.H. Yang, X. Wang, P.C. Stancil, J.M. Bowman, N. Balakrishnan, R.C. Forrey, J. Chem. Phys. 145 (2016) 224307.
[24] B.H. Yang, P. Zhang, X.H. Wang, P.C. Stancil, J.M. Bowman, N. Balakrishnan, B.M. McLaughlin, R.C. Forrey, J. Phys. Chem. A 122 (2018) 1511–1520.
[25] B.H. Yang, P. Zhang, C. Qu, P.C. Stancil, J.M. Bowman, N. Balakrishnan, R.C. Forrey, Phys. Chem. Chem. Phys. 20 (2018) 28425–28434.
[26] D.Z. Yang, J. Huang, X.X. Hu, H. Guo, D.Q. Xie, Nat. Commun. 10 (2019) 4568.
[27] R.C. Forrey, B.H. Yang, P.C. Stancil, N. Balakrishnan, Chem. Phys. 462 (2015) 71–78.
[28] C. Castro, K. Doan, M. Klemka, R.C. Forrey, B.H. Yang, P.C. Stancil, N. Balakrishnan, Mol. Astrophys. 6 (2017) 47–58.
[29] H. Burton, R. Mysliwiec, R.C. Forrey, B.H. Yang, P.C. Stancil, N. Balakrishnan, Mol. Astrophys. 11 (2017) 23–32.
[30] T.B. Adler, G. Knizia, H.-J. Werner, J. Chem. Phys. 127 (2007) 221106.
[31] H.-J. Werner, T.B. Adler, F.R. Manby, J. Chem. Phys. 126 (2007) 164102.
[32] H.-J. Werner, P.J. Knowles, G. Knizia, F.R. Manby, M. Schütz, WIREs Comput. Mol. Sci. 2 (2012) 242.
[33] H.-J. Werner, P.J. Knowles, G. Knizia, F.R. Manby, M. Schütz, P. Celani, et al., MOLPRO, version 2010.1, a package of ab initio programs.http://www.molpro.net.
[34] R.A. Kendall, T.H. Dunning, R.J. Harrison, J. Chem. Phys. 96 (1992) 6796–6806.
[35] T.H. Dunning Jr., J. Chem. Phys. 90 (1989) 1007–1023.
[36] K.A. Peterson, J. Chem. Phys. 117 (2002) 10548.
[37] F. Weigend, A. Köhn, C. Hättig, J. Chem. Phys. 116 (2002) 3175–3183.
[38] C. Hättig, Phys. Chem. Chem. Phys. 7 (2005) 59–66.
[39] D. Feller, K.A. Peterson, J.G. Hill, J. Chem. Phys. 133 (2010) 84102.
[40] S.F. Boys, F. Bernardi, Mol. Phys. 19 (1970) 553–566.
[41] B.J. Braams, J.M. Bowman, Int. Rev. Phys. Chem. 28 (2009) 577.
[42] J.M. Bowman, B.J. Braams, S. Carter, et al., J. Phys. Chem. Lett. 1 (2010) 1866–1874.
[43] Z. Xie, J.M. Bowman, J. Chem. Theory Comput. 6 (2010) 26–34 URL: Seehttps://scholarblogs.emory.edu/bowman/msa/.
[44] R.V. Krems, TwoBC – Quantum Scattering Program, University of British Columbia, Vancouver, Canada, 2006.
[45] G. Quéméner, N. Balakrishnan, J. Chem. Phys. 130 (2009) 114303.
[46] S.J. Green, Chem. Phys. 62 (1975) 2271–2277.
[47] B.R. Johnson, J. Comput. Phys. 13 (1973) 445–449.
[48] Q. Qian, C.L. Yang, F. Gao, X.Y. Zhang, Acta Phys. Sin. 56 (2007) 4420.
[49] D.W. Schwenke, J. Chem. Phys. 89 (1988) 2076–2091.
[50] N. Balakrishnan, A. Dalgarno, R.C. Forrey, J. Chem. Phys. 113 (2000) 621–627.
[51] N. Balakrishnan, G.C. Groenenboom, R.V. Krem, A. Dalgarno, J. Chem. Phys. 118 (2003) 7386–7393.
[52] M. Agúndez, V. Wakelam, Chem. Rev. 113 (2013) 8710–8737.
[53] M. Agúndez, N. Marcelino, J. Cernicharo, E. Roueff, M. Tafalla, Astron. Astrophys. 625 (2019) A147.
[54] J.-C. Loison, V. Wakelam, P. Gratier, et al., Mon. Notices R. Astron. Soc. 485 (2019) 5777–5789.
[55] V. Lattanzi, G. Cazzoli, C. Puzzarini, Astrophy. J. 813 (2015) 4.
[56] M.A. Martin-Drumel, F. Hindle, G. Mouret, J. Cernicharo, Astrophys. J. 799 (2015) 115.
[57] S. Pacheco-Vázquez, A. Fuente, C. Baruteau, O. Berné, M. Agúndez, R. Neri, J.R. Goicoechea, J. Cernicharo, R. Bachiller, Astron. Astrophys. 589 (2016) 11.
[58] D. Semenov, C. Favre, D. Fedele, et al., Astron. Astrophys. 617 (2018) A28.